Revision 1

New SIMS reference materials for measuring water in upper mantle minerals

Kathryn M. Kumamoto[1,*], Jessica M. Warren[2], Erik H. Hauri[3]

[1]Department of Geological Sciences, Stanford University, 450 Serra Mall, Bldg 320, Stanford, CA 94305

[2]Department of Geological Sciences, University of Delaware, Penny Hall, 255 Academy Street, Newark, DE 19716

[3]Department of Terrestrial Magnetism, Carnegie Institution of Washington, 5241 Broad Branch Road NW, Washington, DC 20015

*Corresponding author. Email: kkumamot@stanford.edu

Abstract

Trace amounts of water in the nominally anhydrous minerals of the upper mantle can dramatically affect their thermodynamic and rheological properties. Secondary ion mass spectrometry (SIMS) has become a mainstream technique for quantifying small amounts of water in these minerals, but depends on standards with known concentrations of water. The current standards in use for mantle minerals are well-characterized (Hauri et al., 2002; Koga et al., 2003; Aubaud et al., 2007; Mosenfelder and Rossman, 2013a, 2013b), but a lack of extra material has limited the spread of this technique to other laboratories.

We present new SIMS measurements on natural mantle xenolith pyroxenes that are suitable for use as calibration reference materials. They are calibrated off of the pyroxene standards currently in use at the Department of Terrestrial Magnetism of the Carnegie Institution

of Washington (Koga et al., 2003; Aubaud et al., 2007). They have homogeneous water contents, defined as a standard deviation of < 10% for analyses across multiple grains. Reference materials for H_2O cover ranges from 52 to 328 ppm and from 9 to 559 ppm in orthopyroxene and clinopyroxene respectively, covering most of the observed range of mantle water contents. The samples are evenly distributed over those ranges. The orthopyroxene reference materials can also be used to measure water in olivine based on previous observations that these two minerals have similar calibration slopes.

The new pyroxene reference materials can also be used to calibrate fluorine and phosphorus at low concentrations. We found that fluorine in particular was homogeneous in both orthopyroxene and clinopyroxene, with concentrations of 3 to 50 ppm in orthopyroxene and 0.5 to 118 ppm in clinopyroxene. Phosphorus ranges from below detection up to 19 ppm in orthopyroxene and up to 73 ppm in clinopyroxene, but was more heterogeneous within some samples. Most of the reference materials have concentrations at the lower end of the ranges for fluorine and phosphorus in this study, with only a few samples showing higher concentrations.

Keywords: SIMS, calibration, water, volatiles, nominally anhydrous minerals

Introduction

The upper mantle is largely composed of the nominally anhydrous minerals (NAMs) olivine, orthopyroxene, and clinopyroxene. Water can occur as a trace element in these minerals, dissolved as hydroxyl groups bonded in the crystal structure (e.g., Smyth et al., 1991; Wright and Catlow, 1994; Bell et al., 1995; Stalder et al., 2005). The presence of small amounts of water in NAMs influences both physical and chemical properties, including viscosity (e.g., Mackwell et

al., 1985; Karato et al., 1986; Hirth and Kohlstedt, 1996; Mei and Kohlstedt, 2000), melting temperature (e.g., Kushiro et al., 1968), electrical conductivity (e.g., Karato, 1990; Schlecter et al., 2012; Sarafian et al., 2015), and seismic wave velocity (e.g., Katayama et al., 2004). The amount of water present in the mantle is poorly constrained, with estimates for total water stored in the mantle varying from 0.25 to 4 times the mass of water in all the Earth's oceans (Hirschmann, 2006). Studies have also shown that water distribution is heterogeneous throughout the mantle (e.g., Peslier, 2010; Warren and Hauri, 2014). To quantify and study the effects of variable amounts of water on mantle properties, techniques are needed to measure very small concentrations of volatiles in NAMs.

Fourier transform infrared spectroscopy (FTIR) has been the most common method used to measure water in NAMs (e.g., Peslier, 2010). This technique is ideal for determining site occupancy and can be used to derive absolute concentration as well. However, sample preparation is arduous as it requires doubly polished, oriented grains (e.g., Libowitzky and Rossman, 1996; Bell et al., 2003). In addition, subtracting the background signal from this spectroscopic technique can be time-consuming and difficult to quantify and reproduce. For example, iron-bearing orthopyroxene and clinopyroxene both have very complex curved baselines (e.g., Goldman and Rossman, 1976; Bell et al., 1995; Mosenfelder and Rossman, 2013a, 2013b). Calibration of FTIR spectra is also subject to uncertainty, including which peaks should be used to calculate concentration, whether or not the spectra should be polarized, and whether a mineral-specific or frequency-dependent calibration is most appropriate (e.g., Libowitzky and Rossman, 1997; Withers et al., 2012; Mosenfelder and Rossman, 2013a, 2013b). In particular, the calibration for olivine, the most common mineral in the upper mantle of the Earth, is the subject of considerable debate (e.g., Bell et al., 2003; Aubaud et al., 2009; Kovács et

al., 2010; Mosenfelder et al., 2011; Withers et al., 2012).

Over the last 15 years, secondary ion mass spectrometry (SIMS) has become a mainstream technique for measuring water in NAMs (e.g., Koga et al., 2003; Hauri et al., 2006; Aubaud et al., 2007; Ludwig and Stalder, 2007; Mosenfelder et al., 2011; Stalder et al., 2012; Withers et al., 2012; Mosenfelder and Rossman, 2013a, 2013b). SIMS requires only a single polished surface on an unoriented grain in order to measure water concentration, making the sample preparation far easier. Traditionally, SIMS has had a relatively high detection limit for hydrogen, making analysis of water in NAMs difficult. Improvements in sample preparation and analytical conditions, however, mean that detection limits can now be as low as a few ppm H_2O (e.g., Le Voyer et al., 2015).

As a mass spectrometry technique, SIMS necessarily depends on standards with predetermined water concentrations in order to accurately measure absolute concentrations of water in unknowns. Standards must be matrix-matched since the structure and chemistry of the substrate can have large effects on how easily different elements are ionized by the primary beam of the ion probe (e.g., Deline et al., 1978; Hauri et al., 2002). The standards in use today for olivine, orthopyroxene, and clinopyroxene (e.g., Koga et al., 2003; Aubaud et al., 2007, 2009; Mosenfelder et al., 2011; Mosenfelder and Rossman, 2013a, 2013b; Turner et al., 2015) are well characterized but generally limited in supply, making it difficult for this technique to become more widespread. Standards and analytical protocols also vary between laboratories, potentially leading to difficulties in comparing results.

Here, we present measurements on minerals from natural samples (predominantly peridotite xenolith samples that are large in size) that are suitable as SIMS reference materials for the measurement of water in upper mantle minerals. We also present measurements on

fluorine and phosphorus in these minerals. Finally, we present details of the data collection and processing steps, including a drift correction technique, to establish a standard analytical protocol.

Sample selection

Samples were chosen from a suite of 34 samples representing a variety of ultramafic sources, including peridotite massifs, pyroxene megacrysts, and peridotite xenoliths. Twenty-three samples were loaned from the Department of Mineral Sciences, Smithsonian Institution, of which 13 were selected as reference materials (their Smithsonian ID is included in Table 1). Nine of these 13 samples were previously described for both water content and major element compositions (Luhr and Aranda-Gomez, 1997; Peslier et al., 2002). Three samples from Simcoe were leant by Anne Peslier and Alan Brandon and have also been previously characterized for water content and major elements (Brandon and Draper, 1996; Peslier et al., 2002). Two samples from Kilbourne Hole were donated by Jason Harvey, with major and trace elements presented in Harvey et al. (2012). A peridotite xenolith from San Carlos, AZ was from the collection of J.M. Warren and has not been previously characterized. Three previously uncharacterized pyroxenes were obtained from the Stanford Mineral Collection, and two were selected as reference materials. In addition, three megacrysts gathered from the Trinity and Josephine Ophiolites were analyzed but proved too altered for use as reference materials.

In total, 15 orthopyroxene and 12 clinopyroxene reference materials were chosen based on high sample abundance, minimal levels of alteration, and homogeneity in pyroxene water content. Table 1 provides a summary of sample mineralogies and localities. For samples where pyroxene chemistry had not been analyzed, we used the JEOL JXA-8230 Electron Microprobe at

Stanford University to measure the abundances of major elements Si, Al, Ti, Cr, Mn, Mg, Ca, Fe, Na, and Ni. Current was maintained at 30 nA using a 15 kV beam and an 8 μm spot size. Ten adjacent analyses were gathered perpendicular to any apparent exsolution lamellae on each grain in order to constrain sample chemistry.

All pyroxenes are plotted in Figure 1 on a pyroxene Mg-Ca-Fe ternary, and a compilation of their major element chemistry is provided in Supplement 1. For all samples presented here, orthopyroxene compositions correspond to predominantly enstatite with small amounts of iron and calcium. Al_2O_3 concentrations range from 1.9 to 5.6 wt%. Clinopyroxene compositions are generally chrome diopside with some variation in the amount of calcium incorporated. Aluminum contents cover a larger range for clinopyroxene than orthopyroxene, varying between 0.1 and 7.7 wt%. These compositions fall within the range of typical mantle pyroxenes (grey background points in Figure 1), with the exception of one diopside, SMC31139. This mineral specimen is from a nickel mine bordering a hydrothermally-altered serpentinite (see Tarassoff and Gault, 1994, for a summary of the geology of the mine) and is a 4:1 diopside:hedenbergite solid solution (Figure 1).

Secondary ion mass spectrometry

Sample preparation

To prepare mounts for SIMS analyses, xenoliths and megacrysts were lightly crushed, and grains of each mineral phase were picked based on optical purity. Grains were cleaned by sonicating in DI water for 1 minute before rinsing in ethanol and drying overnight. To create a mount, grains were pressed into indium-filled 1-inch aluminum rounds (e.g., Koga et al., 2003; Aubaud et al., 2007). A grain of Suprasil 3002 glass (1 ppm H_2O certified by Heraeus Quarzglas)

or synthetic forsterite (0.04 ppm H_2O, Koga et al., 2003) was included in each mount for measuring the background water content of the instrument. Suprasil glass in particular had reproducible low water concentrations, making it the recommended material for use as a blank. A grain of ALV-519-4-1 basaltic glass was also always included to track instrumental drift over the course of a session. Mounts were ground by hand with SiC sandpaper to expose the approximate center of each grain. They were then polished using diamond solutions down to a 1 μm polish before being cleaned again with DI water and ethanol.

Analytical conditions

Water concentrations in NAMs were measured in mineral grains using the Cameca IMS 6f ion microprobe at the Department of Terrestrial Magnetism (DTM), Carnegie Institution of Washington. Data for this study were gathered over three analytical sessions in July 2014, April 2015, and January 2016. Prior to analysis, mounts were stored in a vacuum oven at 50˚C for at least 12 hours, then removed and coated with ~40 nm of gold. Samples were introduced into the exchange chamber at least 24 hours before being moved into the main chamber in order to maintain the ultrahigh vacuum ($P < 10^{-9}$ torr) necessary for measuring volatiles in nominally anhydrous minerals.

Analyses were made using a rastered Cs^+ beam with a current of 15-25 nA and an accelerating voltage of 10 kV. Charge compensation was provided by an electron flood gun. The sputter pits typically measure ~30-40 μm in diameter, but counts were only collected from the center 10 μm of each pit by using the smallest field aperture. After five minutes of presputtering, the magnet was cycled through masses ^{12}C, $^{16}O^1H$, ^{19}F, ^{30}Si, ^{31}P, ^{32}S, and ^{35}Cl. Counting times were 10s for ^{12}C and 5s for all other masses. Five cycles of data were collected per analysis using the electron multiplier, and a deadtime correction was automatically applied. The blank (Suprasil

3002 glass or synthetic forsterite) and secondary standard (ALV-519-4-1) were measured every 10-20 analyses.

Calibration

Standards from Hauri et al. (2002), Koga et al. (2003), and Aubaud et al. (2007) were run at the beginning of each analytical session. The basaltic glass standards ALV-519-4-1, WOK-28-3, ALV-1654-3, ALV-1833-1, ALV-1833-11, and ALV-1846-12, calibrated by Hauri et al. (2002), were run first. Volatile concentrations and silica contents for these glasses are listed in Table 2. Since these glasses contain higher concentrations of water than the NAM standards, they are generally easier to measure and a good first estimate of machine conditions.

Standards used for measuring water in orthopyroxene were Opx A288, India Enstatite, KBH- 1, and ROM-273-OG2. Clinopyroxene standards were ROM-271-10, PMR-53, ROM-271-16, and ROM-271-21. Compositions and references for these standards are in Table 3. Most of these standards have been calibrated with FTIR (Koga et al., 2003; Aubaud et al., 2007). Importantly, however, the orthopyroxene KBH-1 and the clinopyroxene PMR-53 were measured by vacuum manometry by Bell et al. (1995) and thus provide calibration anchor points that are independent of FTIR integration methods and choice of absorption coefficients. PMR-53 is known to fall off the calibration curve for clinopyroxene (possible reasons are discussed in Mosenfelder and Rossman, 2013b), but until more absolute measurements of water in clinopyroxene are made, this remains an unresolved issue.

Calibration curves were constructed using a weighted least squares linear regression of water content versus the $^{16}O^{1}H/^{30}Si$ counts ratio and forced through the origin. The regression was done in MATLAB using the function *lscov* with a weight assigned to each point. Weighting was based on the uncertainty in the accepted FTIR or manometry values for water content. The

uncertainty in the $^{16}O^{1}H/^{30}Si$ count ratio was excluded because it was much smaller than the uncertainty in the accepted values. The 1σ standard error on the calibration slope was typically around 4% for orthopyroxene and around 12% for clinopyroxene. The higher error in the slope for the clinopyroxene calibration was due to the relatively wide spread of standards around the calibration line, a consistent characteristic of these standards also observed by Mosenfelder and Rossman (2013b).

Water contents of one of the orthopyroxene standards (India Enstatite) and three of the clinopyroxene standards (PMR-53, ROM-271-16, and ROM-271-21) were analyzed by Aubaud et al. (2009) using three different FTIR calibrations (Paterson, 1982; Bell et al., 1995; Libowitzky and Rossman, 1997), as well as by elastic recoil detection analysis (ERDA). Since India Enstatite is the only common orthopyroxene standard between Aubaud et al. (2009) and the DTM standards used in this study, we have used the values for this standard from Koga et al. (2003), which is based on the Bell et al. (1995) FTIR calibration for orthopyroxene (Table 3). For clinopyroxene, the results of the Aubaud et al. (2009) analyses differ dramatically from each other depending on the FTIR calibration and the technique, similar to the results of Mosenfelder and Rossman (2013b) on an overlapping set of standards. These differences have large effects on the calculated calibration slope, and thus the calculated water contents of new samples. We have chosen to continue using values calculated by Koga et al. (2003) and Aubaud et al. (2007) based on the Bell et al. (1995) FTIR calibration (Table 3). This allows for direct comparisons to be made with many FTIR datasets for water in diopsides and calcium-rich augites, which mainly use the Bell calibration (e.g., Grant et al., 2007; Bonadiman et al., 2009; Xia et al., 2010; Doucet et al., 2014; Peslier and Bizimis, 2015). Published SIMS datasets also often use standards based on the Bell et al. (1995) calibration to measure water in pyroxenes (e.g., Warren and Hauri,

208 2014).

209 Since matrix-matched standards do not yet exist for other volatiles in mantle minerals, we
210 used the basaltic glass standards run at the beginning of each session to quantify the
211 concentrations of fluorine and phosphorus (Table 2). As with the water calibrations, these data
212 were fit with a weighted least squares linear regression to create the fluorine and phosphorus
213 calibrations.

214 **Data processing**

215 To process the SIMS data, the following steps were completed: 1) removal of bad data
216 cycles and ratioing of volatile counts to ^{30}Si counts, 2) background correction, 3) instrumental
217 drift correction by analysis number and by mount, 4) filtering of data for statistical anomalies
218 and contamination, and finally, 5) application of the calibration curve to calculate final
219 concentrations.

220 Volatile counts were initially ratioed to ^{30}Si as a first step to average out the effects of
221 instrument drift. Fluctuations in primary ion beam current during a single analysis can result in
222 changes in count magnitude for all species measured. By ratioing to ^{30}Si, the effects of such
223 fluctuations are mitigated. Bad data cycles, the result of an electronic glitch in the DTM 6f
224 SIMS, were identified as a drop to near zero counts for one mass in a single cycle. These cycles
225 were removed.

226 Synthetic forsterite or Suprasil 3002 glass (depending on the mount) was used to measure
227 the background volatile content of the instrument. These grains were measured regularly during
228 each session, and the average background count ratios for a mount were calculated. The ratios
229 $^{16}OH^{1}/^{30}Si$, $^{19}F/^{30}Si$, and $^{31}P/^{30}Si$ were then used to correct for background water, fluorine, and
230 phosphorus by subtracting the mount average background from each individual unknown

231 measurement on the mount.

232 We used analyses of basaltic glass ALV-519-4-1 as a secondary standard to further
233 account for instrumental drift as well as changes in instrumental conditions between mounts.
234 This secondary standard has proven to be a very reproducible, homogeneous standard for all
235 elements measured under the above analytical conditions. Le Voyer et al. (2015) report a
236 standard deviation <2.5% for all volatiles in ALV-519-4-1 for >250 analyses collected over two
237 years. If instrument conditions do not change over the course of an analytical session, ALV-519-
238 4-1 analyses should always have the same count ratios throughout the session. Since instrument
239 conditions do change, for instance due to putting in a new mount or refocusing the primary
240 beam, the secondary standard is used to correct for instrumental drift among analyses in a single
241 mount, as well as differences between mounts (K-factor correction). Mathematical details of the
242 two ALV-519-4-1 corrections are provided in the appendix.

243 Instrumental drift between analyses on an individual mount was identified as linear trends
244 in volatile count ratios in the glass against analysis number, which is a proxy for time. This drift
245 was removed using a percentage correction function and was applied to every analysis, including
246 analyses of ALV-519-4-1. The correction nearly always recovers values for ALV-519-4-1 that
247 are within 10% of the average count ratio for analyses of ALV- 519-4-1 on a given mount. A
248 new correction function was used for each indium mount, and a new correction function was
249 usually calculated every day for mounts that ran over multiple days.

250 The K-factor correction was then applied after the drift correction to account for
251 differences in count ratios between mounts, which are ultimately due to changes in instrument
252 conditions when the mount is changed. This was done by calculating the percent change required
253 to bring the ALV-519-4-1 analyses on the unknown mount into agreement with the ALV-519-4-

1 analyses on the standard mount (upon which the calibration is based) and applying that percentage change to all analyses on the unknown mount. This correction makes the average $^{16}O^{1}H/^{30}Si$ ratio of ALV-519-4-1 for each new mount equal the value for ALV-519-4-1 run during the standard calibration.

Standard analyses during one session - conducted in April 2015 - resulted in calculated values for H_2O in ALV-519-4-1 that were anomalously high by 5.3% (relative) compared with other analytical sessions before and afterward. As a result, the K-factor correction for all analyses in the April 2015 session was reduced by 5.3% in order to bring the calculated H_2O values for ALV-519-4-1 into consistency with other analytical sessions.

The ratios $^{12}C/^{30}Si$, $^{32}S/^{30}Si$, and $^{35}Cl/^{30}Si$ were used to monitor for compromised analyses. High counts in any of these elemental ratios are assumed to indicate interference from surface contamination, inclusions, fracture material, or alteration, and these analyses were discarded. Points with variable $^{16}O^{1}H/^{30}Si$ count ratios (>1.5% error as measured over 5 cycles) were also removed from the final data set. Data reduced to this point are reported in Supplement 3.

In the final step of data processing, the calibrations were applied to the remaining analyses to calculate the concentrations of volatiles in the unknowns. For all samples, this was done by multiplying the corrected volatile count ratios by the slope of the appropriate calibration line. Calibration data for each session are reported in Supplement 3.

Results

The results of our SIMS analyses are presented in Table 4. The data are plotted in Figures 2 and 3 as box-and-whisker plots of all good analyses across all grains on a sample-by-sample

277 basis. In these plots, the boxes contain 50% of the analyses centered around the median, while
278 the whiskers show the range of all analyses. Some samples show larger variability in water
279 content than others, but all fall under the 10% standard deviation cut-off imposed as a measure of
280 homogeneity.

281 Water contents in orthopyroxene range from 52 to 328 ppm, while the range in
282 clinopyroxene is from 9 to 559 ppm. Reference materials are relatively evenly distributed across
283 the range in water contents for each phase (Figure 2). Fluorine varies between 3.0 and 50.3 ppm
284 in orthopyroxene and between 0.5 and 118.2 in clinopyroxene, while phosphorus concentrations
285 range from below detection to 18.6 ppm in orthopyroxene and to 72.8 ppm in clinopyroxene
286 (Figure 3). Water does not exhibit any covariation with either of these two elements.
287 Concentrations are generally homogeneous for both elements, but a few samples show large
288 compositional variations in phosphorus while maintaining homogeneity in water and fluorine.

289 Table 4 presents error calculated in two ways: 1) the standard deviation of repeat analyses
290 on grains from the same sample, and 2) the propagated uncertainties of the final values, taking
291 into account the uncertainty in the blank measurement and the uncertainty on the slope of the
292 DTM calibration line. The first error estimate, based on repeat analyses of a sample, provides the
293 best representation of reproducibility. This estimate was used to determine the homogeneity of
294 each sample. As the goal of this study is to create new reference materials for SIMS analyses of
295 water concentration in NAMs, samples were only selected as reference materials, and thus
296 reported here, if they are homogeneous with respect to water, with a standard deviation of less
297 than 10% amongst analyses on multiple grains. A minimum of ten analyses over at least two
298 grains was required for this criteria, with up to 134 analyses over 8 grains for an individual
299 sample (KH03-27 orthopyroxene) in this study. The second method for estimating error provides

a more accurate representation of the uncertainty in absolute concentration as it accounts for the uncertainties in the DTM calibration.

Table 4 also reports the number of analyses that passed all data reduction tests and thus contribute to the final values for each volatile. The percentage of total analyses represented by this subset is also reported. The discarded analyses are ones that were classified as compromised due to high counts of C, S or Cl, or variable OH ratios during analysis. Based on petrographic examination, a small number of samples contain fluid inclusions, mainly concentrated along microcracks (Figure 4) and possibly following specific crystallographic planes. Inclusions are not present in all grains, however, and all of the crystals we examined have large clean areas with no inclusions. If the primary ion beam hits an inclusion, either solid or fluid, fluctuations occur in water content over the course of the five data cycles and/or detectable amounts of carbon, sulfur, or chlorine are found. These types of analyses are removed by the data reduction routine.

For example, sample 117322-242 contains small inclusions that can be seen with scanning electron microscopy. The comparatively low percentage of good analyses (62.5%) for this diopside megacryst is indicative of the high number of inclusions in this sample. However, the narrow spread of water content over the 25 good analyses of 117322-242 (4% 1σ standard deviation) is also indicative of a high degree of sample homogeneity away from the inclusions and that our data processing easily removes bad analyses. We expect that alteration (e.g. serpentine or amphibole) would be similarly simple to detect, though the samples presented in this study show little evidence for any pervasive alteration.

Discussion

323 **Calibration reference materials for water**

324 We have created a new set of pyroxene calibration reference materials for SIMS
325 measurements of volatiles in mantle NAMs (Table 4, Figures 2 and 3). These reference materials
326 are suitable for the calibration of water in olivine as well as pyroxene, as olivine has the same
327 calibration slope as orthopyroxene (Koga et al., 2003; Kovács et al., 2010; Withers et al., 2011;
328 Mosenfelder and Rossman, 2013a; Warren and Hauri, 2014). For each sample, we have
329 characterized several grains of each phase and used this to select reference materials that have
330 homogeneous water contents within 10% standard deviation and no detectable diffusional
331 gradients outside of error. Occasionally in these grains, an individual analysis may appear
332 anomalously high or low compared to other repeat analyses, despite looking like a good analysis
333 according to the data reduction process. For calibration purposes, if an individual analysis falls
334 far away from other repeat analyses, it should be removed from the calibration curve.

335 While our standard deviation values (Table 4) are larger than those of current standards
336 (Koga et al., 2003; Aubaud et al., 2007; Mosenfelder and Rossman, 2013a, 2013b), our samples
337 have a larger number of repeat measurements over multiple grains and multiple sessions. The
338 opportunity to collect so many data points allows us to better estimate the uncertainty in
339 concentrations.

340 Data are also presented on a grain-by-grain basis in Supplemental Figure 1 and
341 Supplemental Table 2. In general, averages by grain have lower standard deviations than the
342 averages by sample, most likely due to all points on a grain being measured consecutively within
343 a short time period during a session. Any instrumental drift during this time should be negligible,
344 whereas changes in conditions between grains on the same mount, on different mounts, and
345 during different sessions could be far larger. The observed intergranular variations may also be

346 due to real variations in water content, and the potential always exists that other grains may show
347 resolvable zonation within the sample. Therefore, when using these samples as reference
348 materials, we recommend using the sample averages and propagated uncertainties for calculating
349 calibration curves, as these values account for more possible sources of uncertainty and better
350 represent the intra- and inter-session behavior of these materials.

351 To confirm the validity of our new reference material set, a subset of the orthopyroxene
352 samples were run in conjunction with the DTM standards on the Stanford University Cameca
353 NanoSIMS 50L using a 10 nA Cs+ beam and an accelerating voltage of 8 kV. After a 3-minute
354 presputter on a 30 x 30 μm area, analyses were collected on a centered 10 x 10 μm raster with
355 electronic gating to the central 3 x 3 μm area. Masses were collected simultaneously using a
356 multi-collector, with five blocks of ten frames each gathered in 50 seconds. After a correction
357 using ALV-519-4-1 to bring count ratios across the mounts into alignment, the two sets of
358 calibration materials produced nearly identical calibration curves (Figure 5).

359 Our reference materials are unusual in that we are using water concentrations determined
360 by SIMS to create new reference materials for SIMS. The absolute concentration of water in
361 calibration standards are more typically measured using alternative techniques, such as FTIR,
362 ERDA, nuclear reaction analysis (NRA), or hydrogen manometry (e.g., Koga et al., 2003;
363 Aubaud et al., 2007; Mosenfelder et al., 2011; Mosenfelder and Rossman, 2013a, 2013b; Turner
364 et al., 2015). However, each of these techniques has its own drawbacks. Hydrogen manometry,
365 for instance, requires a large sample of clean material that is destroyed in the process of making
366 the measurement (e.g., Rossman, 2006). ERDA generally has a high background water content,
367 as observed by Aubaud et al. (2009), making measurements of very low water concentrations,
368 such as those present in natural mantle olivine, difficult. NRA can achieve very low detection

limits (e.g., Endisch et al., 1994; Bell et al., 2003; Maldener et al., 2003) but is not easily accessible. FTIR, as mentioned earlier, suffers from difficulties in selecting the proper calibration, proper removal of background, and time-intensive sample preparation.

We purposely only calibrated our reference materials against the DTM standards, meaning they are entirely dependent on the values of those standards, which were calibrated by Bell et al. (1995), Hauri et al. (2002), Koga et al. (2003), and Aubaud et al. (2007). This means that any future revisions to the DTM standard values will be straightforward to propagate through our reference material values. The standards in use at DTM (Bell et al., 1995; Hauri et al., 2002; Koga et al., 2003; Aubaud et al., 2007) and Caltech (Mosenfelder et al., 2011; Mosenfelder and Rossman, 2013a, 2013b) currently represent the best-constrained set of standards that we are aware of for the analysis of water in olivine and pyroxenes via SIMS. These standards include two grains with manometry measurements of water content by Bell et al. (1995): the orthopyroxene KBH-1 and the clinopyroxene PMR-53. However, most of the DTM standards were calibrated via FTIR and may be subject to future revisions, particularly as more research is done into mineral-specific versus frequency-dependent calibrations and the background correction. Solving these problems will require more absolute measurements of water (e.g., by ERDA, NRA, or manometry). When this occurs, the water concentrations of the reference materials presented here could be revised by calculating a new calibration curve based on updated values for the original DTM standards. This situation would only require re-processing of the final step of the data reduction to apply the updated calibration, and the data necessary for this are provided in Supplementary Table 3. Updating the calibration would result in a shift in the absolute value of samples, but observations of relative variability among samples would remain unchanged. As the accuracy of the calibration curves improves, the error

associated with SIMS analyses will be reduced.

A subset of our reference materials have been previously measured by FTIR by Peslier et al. (2002). Our values for this sample subset are offset from those of Peslier et al. (2002), as shown in Figure 6. For clinopyroxene, this offset is fairly minor and randomly distributed about the 1:1 line. In contrast, orthopyroxene shows a systematic offset with almost all SIMS data having higher concentrations than the FTIR data (Figure 6). As Peslier et al. (2002), Koga et al. (2003), and Aubaud et al. (2007) all use the Bell et al. (1995) mineral-specific calibrations, we attribute the discrepancy between our SIMS values and the Peslier et al. (2002) values to the method of FTIR background removal. In Peslier et al. (2002), the background was determined by experimentally dehydrating a single xenolith sample and using FTIR spectra gathered from this sample as the background for all samples in the study. Each mineral phase in each xenolith has its own baseline, however, due to influences from composition, oxidation state, and precise orientation of the grain. Thus, using dehydration spectra to determine baselines would be better done by dehydrating a grain of each mineral for each sample (Peslier, personal communication). Koga et al. (2003) and Aubaud et al. (2007), on the other hand, both employed a polynomial baseline fit to remove the background of samples in their studies. Given the uncertainty of previous work, future FTIR work on the samples in this study may resolve the offset seen between the FTIR and SIMS measurements.

Fluorine and phosphorus

The fluorine and phosphorus data presented in this study allows these samples to be used as reference materials for low concentrations of these elements. Most of the samples are homogeneous for fluorine (Figure 3), with a standard deviation ranging from 2 to 7% (1σ) for orthopyroxene and clinopyroxene, except for two low-fluorine orthopyroxenes (Table 4).

Phosphorus, on the other hand, is homogeneous in some of our samples, but highly heterogeneous in others (Figure 3), with the standard deviation for a sample ranging from 2-150% (1σ; Table 4). For both elements in both phases, however, a subset of the reference materials have <10% 1σ standard deviation and can be used to create a calibration curve suitable for low concentrations of fluorine and phosphorus. For higher concentrations, a basaltic glass calibration should be used.

The overall issue with the fluorine and phosphorus calibrations is the lack of independently calibrated pyroxenes, resulting in calibration curves that are not matrix-matched to pyroxenes. We used a set of basaltic glasses to create calibration curves for these elements (Table 2). These glass standards were calibrated off of another set of four glass standards with known fluorine concentrations (Hauri et al., 2002). We chose not to scale our calibrations to the glass silica contents in the manner of Mosenfelder and Rossman (2013a, 2013b), because a scaling correction is not clearly necessary based on the limited dataset. The difference in final concentrations of fluorine and phosphorus in the pyroxenes between a calibration scaled with silica content in the glasses and pyroxenes versus a calibration not scaled with silica is very minor (~2.5%). Once standards have been analyzed for fluorine and phosphorus by an independent method, the calibration procedure here can be updated to incorporate scaling with silica content if appropriate.

Fluorine concentrations in orthopyroxene and clinopyroxene cover a range (opx = 3.0-50.3 ppm; cpx = 0.5-118.2) similar to that seen by Gazel et al. (2012) in mantle xenoliths (opx = 13-43 ppm; cpx = 30-111 ppm) and Warren and Hauri (2014) in peridotites from a variety of tectonic settings (opx = 0.2-26 ppm; cpx = 0.1-66 ppm). Recent observations of fluorine in mantle xenoliths extend to higher concentrations than those observed here, with values of up to

200 ppm in pyroxenite veins (e.g., Rooks et al., 2015). The range of phosphorus concentrations in abyssal peridotites studied by Warren and Hauri (2014) (opx = 1-12 ppm; cpx = 5-32 ppm) is similar to that reported here (opx = b.d.-18.6; cpx = b.d.-72.8). However, Brunet and Chazot (2001), Witt-Eickschen and O'Neill (2005), and Mallmann et al. (2009) measured phosphorus concentrations in peridotite xenoliths that are beyond the range represented in our reference materials (combined range of these sources: opx = 5-40 ppm, cpx = 9-148 ppm).

As previously mentioned, some of the pyroxenes have very variable phosphorus content. Zoning in phosphorus content is well known in igneous olivine, which also has an overall higher abundance of phosphorus, and this zoning is often attributed to complex crystallization processes (e.g. Toplis et al., 1994; Milman-Barris et al., 2008; Welsch et al., 2014; Watson et al., 2015). Mallmann et al. (2009) found phosphorus zoning in mantle olivine from Australian xenoliths and suggested that the patterns were due to metasomatism and deformation. Notably, however, Mallmann et al. (2009) saw no apparent zoning of phosphorus in the pyroxenes from those same samples. The variability in the phosphorus data we present here suggests that zoning may be important in some xenoliths and is worth future exploration.

Volatile partitioning

We examined the partitioning behavior of volatiles between orthopyroxene and clinopyroxene in the seven samples where both phases were present, measured, and homogeneous. In Figure 7, volatile concentrations in clinopyroxene are plotted against orthopyroxene and compared to other datasets. For water, our data falls in the same range as that seen in a literature compilation of natural samples (Bell and Rossman, 1992; Peslier et al., 2002; Demouchy et al., 2006; Aubaud et al., 2007; Grant et al., 2007; Falus et al., 2008; Li et al., 2008; Yang et al., 2008; Bonadiman et al., 2009; Xia et al., 2010; Yu et al., 2011; Hao et al., 2012;

461 Peslier et al., 2012; Denis et al., 2013; Xia et al., 2013; Hao et al., 2014; Warren and Hauri,
462 2014; Bizimis and Peslier, 2015; Hui et al., 2015; Peslier and Bizimis, 2015; Hao et al., 2016).
463 The partition coefficient obtained from this literature compilation is 2.4 ± 0.9. The high
464 uncertainty reflects the variety of methods, localities, and degrees of sample dehydration or
465 alteration present in this compilation. Experimental partition coefficients measured by Aubaud et
466 al. (2004), Hauri et al. (2006), Tenner et al. (2009), and Rosenthal et al. (2015) are lower than
467 that observed in natural samples, at $D^{cpx/opx}_{H2O}$ = 1.3 ± 0.2. Potential reasons for this offset
468 include major element chemistry differences between natural and experimental samples or
469 differences in the pressures and temperatures that natural versus experimental samples
470 experienced (e.g., Warren and Hauri, 2014).

471 The dataset for fluorine partitioning between orthopyroxene and clinopyroxene is much
472 smaller than that for water. A literature compilation of natural samples (Gazel et al., 2012;
473 Warren and Hauri, 2014) combined with our dataset yields a partition coefficient of 3.0 ± 1.0
474 (Figure 7b). Similar to water, the partition coefficient determined by experiments (Dalou et al.,
475 2012; Rosenthal et al., 2015) is smaller than that seen in natural samples, averaging $D^{cpx/opx}_{F}$ =
476 1.5 ± 0.6.

477 The phosphorus dataset for natural mantle samples in the literature is also limited and
478 shows a larger amount of scatter than fluorine (Figure 7c). The combination of our data with
479 other studies measuring phosphorus in natural mantle samples (Witt-Eickschen and O'Neill,
480 2005; Mallman et al., 2009; Gazel et al., 2012; Warren and Hauri, 2014) results in a partition
481 coefficient of 2.7 ± 1.3. Possible reasons for the scatter in this dataset, and thus the high
482 uncertainty in this partition coefficient, include a change in substitution mechanism, as suggested
483 by Witt-Eickschen and O'Neill (2005) and supported by Mallmann et al. (2008), zoning in

484 phosphorus content as suggested by the data presented here, or disequilibrium in phosphorus
485 content due to diffusion. We do not know of any experimental partition coefficients for
486 phosphorus between orthopyroxene and clinopyroxene.
487

488 **Implications**

489 We have produced a set of natural reference materials for measuring volatiles,
490 particularly water, in mantle minerals via SIMS in order to facilitate the use of this technique at
491 more laboratories around the world. We have created a calibration mount of previously analyzed
492 grains of orthopyroxene and clinopyroxene, along with a set of basaltic glasses and a Suprasil
493 3002 glass blank. This calibration mount is available for use in cross-calibrating new grains of
494 these reference materials against the specific grains measured in this study. Sample material is
495 available by request to the Department of Mineral Sciences at the Museum of Natural History,
496 Smithsonian Institution. New grains from these samples should plot within the currently
497 measured water concentration ranges of these samples. However, because intergranular
498 variations are always possible, future grains from these samples should be calibrated against the
499 grains measured in this study.

500 The fluorine and phosphorus contents of the reference materials in this study have also
501 been measured, and fluorine in particular is quite homogeneous. These reference materials can
502 be used to create calibrations for low concentrations of both fluorine and phosphorus, though
503 these calibrations will be no better than ones created using basaltic glass as they are based on
504 glasses. More work must be done to resolve potential matrix effects for these elements, both
505 between glasses with different silica contents and between glass and pyroxene.
506

Acknowledgements

We thank Jason Harvey, Anne Peslier, and Alan Brandon for donating samples for analysis; the Department of Mineral Sciences, Smithsonian Institution, for loaning sample material and Leslie Hale for assisting with access to that material; and Chuck Hitzman for assistance with the NanoSIMS at Stanford. We also thank reviewers Anne Peslier and Jed Mosenfelder and Associate Editor Roland Stalder for their thoughtful comments. This material is based upon work supported by the National Science Foundation under Grant No. EAR-1255620 to JMW and Grant No. EAR-1524581 to EHH, and by the Stanford Nano Shared Facilities through a seed grant to JMW.

References cited

Aubaud, C., Hauri, E.H., and Hirschmann, M.M. (2004) Hydrogen partition coefficients between nominally anhydrous minerals and basaltic melts. Geophysical Research Letters, 31, L20611.

Aubaud, C., Withers, A.C., Hirschmann, M.,M. Guan, Y., Leshin, L.A., Mackwell, S.J., and Bell, D.R. (2007) Intercalibration of FTIR and SIMS for hydrogen measurements in glasses and nominally anhydrous minerals. American Mineralogist, 92, 811–828.

Aubaud, C., Bureau, H., Raepsaet, C., Khodja, H., Withers, A.C., Hirschmann, M.M., and Bell, D.R., (2009) Calibration of the infrared molar absorption coefficients for H in olivine, clinopyroxene and rhyolitic glass by elastic recoil detection analysis. Chemical Geology, 262, 78–86.

Bell, D.R., and Rossman, G.R. (1992) Water in Earth's Mantle: The Role of Nominally Anhydrous Minerals. Science, 255, 1391–1397.

530 Bell, D.R., Ihinger, P.D., and Rossman, G.R. (1995) Quantitative analysis of trace OH in garnet
531 and pyroxenes. American Mineralogist, 80, 465–474.
532 Bell, D.R., Rossman, G.R., Maldener, J., Endisch, D., and Rauch, F. (2003) Hydroxide in
533 olivine: A quantitative determination of the absolute amount and calibration of the IR
534 spectrum. Journal of Geophysical Research, 108, 2105.
535 Bell, D.R., Rossman, G.R., and Moore, R.O. (2004) Abundance and Partitioning of OH in a
536 High-pressure Magmatic System: Megacrysts from the Monastery Kimberlite, South
537 Africa. Journal of Petrology, 45, 1539–1564.
538 Bizimis, M., and Peslier, A.H. (2015) Water in Hawaiian garnet pyroxenites: Implications for
539 water heterogeneity in the mantle. Chemical Geology, 397, 61–75.
540 Bonadiman, C., Hao, Y., Coltorti, M., Dallai, L., Faccini, B., Huang, Y., and Xia, Q. (2009)
541 Water contents of pyroxenes in intraplate lithospheric mantle. European Journal of
542 Mineralogy, 21, 637–647.
543 Brandon, A.D., and Draper, D.S. (1996) Constraints on the origin of the oxidation state of mantle
544 overlying subduction zones: An example from Simcoe, Washington, USA. Geochimica et
545 Cosmochimica Acta, 60, 1739–1749.
546 Brunet, F., and Chazot, G. (2001) Partitioning of phosphorus between olivine, clinopyroxene and
547 silicate glass in a spinel lherzolite xenolith from Yemen. Chemical Geology, 176, 51–72.
548 Bryan, W.B., and Moore, J.G. (1977) Compositional variations of young basalts in the Mid-
549 Atlantic Ridge rift valley near lat 36˚49'N. Geological Society of America Bulletin, 88,
550 556–570.
551 Dalou, C., Koga, K.T., Shimizu, N., Boulon, J., and Devidal, J.-L. (2012) Experimental
552 determination of F and Cl partitioning between lherzolite and basaltic melt. Contributions

553 to Mineralogy and Petrology, 163, 591–609.
554 Deline, V.R., Katz, W., Evans, C.A. Jr., and Williams, P. (1978) Mechanism of the SIMS matrix
555 effect. Applied Physics Letters, 33, 832–835.
556 Demouchy, S., Jacobsen, S.D., Gaillard, F., and Stern, C.R. (2006) Rapid magma ascent
557 recorded by water diffusion profiles in mantle olivine. Geology, 34, 429.
558 Denis, C.M.M., Demouchy, S., and Shaw, C.S.J. (2013) Evidence of dehydration in peridotites
559 from Eifel Volcanic Field and estimates of the rate of magma ascent. Journal of
560 Volcanology and Geothermal Research, 258, 85–99.
561 Doucet, L.S., Peslier, A.H., Ionov, D.A., Brandon, A.D., Golovin, A.V., Goncharov, A.G., and
562 Ashchepkov, I.V. (2014) High water contents in the Siberian cratonic mantle linked to
563 metasomatism: An FTIR study of Udachnaya peridotite xenoliths. Geochimica et
564 Cosmochimica Acta, 137, 159–187.
565 Endisch, D., Sturm, H., and Rauch, F. (1994) Nuclear reaction analysis of hydrogen at levels
566 below 10 at.ppm. Nuclear Instruments and Methods in Physics Research B, 84, 380–392.
567 Falus, G., Tommasi, A., Ingrin, J., and Szabó, C. (2008) Deformation and seismic anisotropy of
568 the lithospheric mantle in the southeastern Carpathians inferred from the study of mantle
569 xenoliths. Earth and Planetary Science Letters, 272, 50–64.
570 Gazel, E., Plank, T., Forsyth, D.W., Bendersky, C., Lee, C.-T.A., and Hauri, E.H. (2012)
571 Lithosphere versus asthenosphere mantle sources at the Big Pine Volcanic Field,
572 California. Geochemistry, Geophysics, Geosystems, 13, 1–25.
573 Goldman, D.S., and Rossman, G.R. (1976) Identification of a Mid-Infrared Electronic
574 Absorption Band of Fe^{2+} in the Distorted M(2) Site of Orthopyroxene, (Mg, Fe)SiO_3.
575 Chemical Physics Letters, 41, 474–475.

576 Grant, K., Ingrin, J., Lorand, J.P., and Dumas, P. (2007) Water partitioning between mantle
577 minerals from peridotite xenoliths. Contributions to Mineralogy and Petrology, 154, 15–
578 34.
579 Hao, Y., Xia, Q., Liu, S., Feng, M., and Zhang, Y. (2012) Recognizing juvenile and relict
580 lithospheric mantle beneath the North China Craton: Combined analysis of H_2O, major
581 and trace elements and Sr-Nd isotope compositions of clinopyroxenes. Lithos, 149, 136–
582 145.
583 Hao, Y., Xia, Q., Li, Q., Chen, H., and Feng, M. (2014) Partial melting control of water contents
584 in the Cenozoic lithospheric mantle of the Cathaysia block of South China. Chemical
585 Geology, 380, 7–19.
586 Hao, Y.-T., Xia, Q.-K., Jia, Z.-B., Zhao, Q.-C., Li, P., Feng, M., and Liu, S.-C. (2016) Regional
587 heterogeneity in the water content of the Cenozoic lithospheric mantle of Eastern China.
588 Journal of Geophysical Research: Solid Earth, 121, 1–21.
589 Harvey, J., Yoshikawa, M., Hammond, S. J., and Burton, K. W. (2012) Deciphering the Trace
590 Element Characteristics in Kilbourne Hole Peridotite Xenoliths: Melt-Rock Interaction
591 and Metasomatism beneath the Rio Grande Rift, SW USA. Journal of Petrology, 53,
592 1709–1742.
593 Hauri, E., Wang, J., Dixon, J.E., King, P.L., Mandeville, C., and Newman, S. (2002) SIMS
594 analysis of volatiles in silicate glasses 1. Calibration, matrix effects and comparisons with
595 FTIR. Chemical Geology, 183, 99–114.
596 Hauri, E.H., Shaw, A.M., Wang, J., Dixon, J.E., King, P.L., and Mandeville, C. (2006) Matrix
597 effects in hydrogen isotope analysis of silicate glasses by SIMS. Chemical Geology, 235,
598 352–365.

599 Hawkins, J.W., Lonsdale, P.F., Macdougall, J.D., and Volpe, A.M. (1990) Petrology of the axial
600 ridge of the Mariana Trough backarc spreading center. Earth and Planetary Science
601 Letters, 100, 226–250.
602 Hirschmann, M.M. (2006) Water, Melting, and the Deep Earth H_2O Cycle. Annual Review of
603 Earth and Planetary Sciences, 34, 629–653.
604 Hirth, G., and Kohlstedt, D.L. (1996) Water in the oceanic upper mantle: implications for
605 rheology, melt extraction and the evolution of the lithosphere. Earth and Planetary
606 Science Letters, 144, 93–108.
607 Hui, H., Peslier, A.H., Rudnick, R.L., Simonetti, A., and Neal, C.R. (2015) Plume-cratonic
608 lithosphere interaction recorded by water and other trace elements in peridotite xenoliths
609 from the Labait volcano, Tanzania. Geochemistry, Geophysics, Geosystems, 16, 1-24.
610 Karato, S. (1990) The role of hydrogen in the electrical conductivity of the upper mantle. Nature,
611 347, 272-273.
612 Karato, S.-i., Paterson, M.S., and Fitzgerald, J.D. (1986) Rheology of Synthetic Olivine
613 Aggregates: Influence of Grain Size and Water. Journal of Geophysical Research, 91,
614 8151-8176.
615 Katayama, I., Jung, H., and Karato, S.-i. (2004) New type of olivine fabric from deformation
616 experiments at modest water content and low stress. Geology, 32, 1045.
617 Koga, K., Hauri, E., Hirschmann, M., and Bell, D. (2003) Hydrogen concentration analyses
618 using SIMS and FTIR: Comparison and calibration for nominally anhydrous minerals.
619 Geochemistry, Geophysics, Geosystems, 4.
620 Kovács, I., O'Neill, H.St.C., Hermann, J., and Hauri, E.H. (2010) Site-specific infrared O-H
621 absorption coefficients for water substitution into olivine. American Mineralogist, 95,

622 292–299.
623 Kushiro, I., Syono, Y., and Akimoto, S.-i. (1968) Melting of a Peridotite Nodule at High
624 Pressures and High Water Pressures. Journal of Geophysical Research, 73, 6023-6029.
625 Le Voyer, M., Cottrell, E., Kelley, K.A., Brounce, M., and Hauri, E.H. (2015) The effect of
626 primary versus secondary processes on the volatile content of MORB glasses: An
627 example from the equatorial Mid-Atlantic Ridge (5˚N-2˚S). Journal of Geophysical
628 Research: Solid Earth, 120, 125-144.
629 Li, Z.-X.A., Lee, C.-T.A., Peslier, A.H., Lenardic, A., and Mackwell, S.J. (2008) Water contents
630 in mantle xenoliths from the Colorado Plateau and vicinity: Implications for the mantle
631 rheology and hydration-induced thinning of continental lithosphere. Journal of
632 Geophysical Research: Solid Earth, 113, B09210.
633 Libowitzky, E., and Rossman, G.R. (1996) Principles of quantitative absorbance measurements
634 in anisotropic crystals. Physics and Chemistry of Minerals, 23, 319–327.
635 Libowitzky, E., and Rossman, G.R. (1997) An IR absorption calibration for water in minerals.
636 American Mineralogist, 82, 1111–1115.
637 Ludwig, T., and Stalder, R. (2007) A new method to eliminate the influence of in situ
638 contamination in SIMS analysis of hydrogen. Journal of Analytical Atomic Spectrometry,
639 22, 1415-1419.
640 Luhr, J.F., and Aranda-Gomez, J.J. (1997) Mexican Peridotite Xenoliths and Tectonic Terranes:
641 Correlations among Vent Location, Texture, Temperature, Pressure, and Oxygen
642 Fugacity. Journal of Petrology, 38, 1075– 1112.
643 Mackwell, S.J., Kohlstedt, D.L., and Paterson, M.S. (1985) The Role of Water in the
644 Deformation of Olivine Single Crytals. Journal of Geophysical Research, 90, 11,319-

11,333.

Maldener, J., Hösch, A., Langer, K., and Rauch, F. (2003) Hydrogen in some natural garnets studied by nuclear reaction analysis and vibrational spectroscopy. Physics and Chemistry of Minerals, 30, 337–344.

Mallmann, G., O'Neill, H.St.C., and Klemme, S. (2009) Heterogeneous distribution of phosphorus in olivine from otherwise well-equilibrated spinel peridotite xenoliths and its implications for the mantle geochemistry of lithium. Contributions to Mineralogy and Petrology, 158, 485–504.

Mei, S., and Kohlstedt, D.L. (2000) Influence of water on plastic deformation of olivine aggregates 2. Dislocation creep regime. Journal of Geophysical Research, 105, 21471–21481.

Milman-Barris, M.S., Beckett, J.R., Baker, M.B., Hofmann, A.E., Morgan, Z., Crowley, M.R., Vielzeuf, D., and Stolper, E. (2008) Zoning of phosphorus in igneous olivine. Contributions to Mineralogy and Petrology, 155, 739-765.

Mosenfelder, J.L., and Rossman, G.R. (2013a) Analysis of hydrogen and fluorine in pyroxenes: I. Orthopyroxene. American Mineralogist, 98, 1026–1041.

Mosenfelder, J.L., and Rossman, G.R. (2013b) Analysis of hydrogen and fluorine in pyroxenes: II. Clinopyroxene. American Mineralogist 98, 1042–1054.

Mosenfelder, J.L., Le Voyer, M., Rossman, G.R., Guan, Y., Bell, D.R., Asimow, P.D., and Eiler, J.M. (2011) Analysis of hydrogen in olivine by SIMS: Evaluation of standards and protocol. American Mineralogist, 96, 1725–1741.

Paterson, M.S. (1982) The determination of hydroxyl by infrared absorption in quartz, silicate glasses, and similar materials. Bulletin of Mineralogy, 105, 20–29.

668 Peslier, A.H. (2010) A review of water contents of nominally anhydrous natural minerals in the
669 mantles of Earth, Mars and the Moon. Journal of Volcanology and Geothermal Research,
670 197, 239–258.
671 Peslier, A.H., and Bizimis, M. (2015) Water in Hawaiian peridotite minerals: A case for a dry
672 metasomatized oceanic mantle lithosphere. Geochemistry, Geophysics, Geosystems, 16,
673 1211–1232.
674 Peslier, A.H., Luhr, J.F., and Post, J. (2002) Low water contents in pyroxenes from spinel-
675 peridotites of the oxidized, sub-arc mantle wedge. Earth and Planetary Science Letters,
676 201, 69–86.
677 Peslier, A.H., Woodland, A.B., Bell, D.R., Lasarov, M., and Lapen, T.J. (2012) Metasomatic
678 control of water contents in the Kaapvaal cratonic mantle. Geochimica et Cosmochimica
679 Acta, 97, 213-246.
680 Rooks, E., Gibson, S., Leat, P., and Petrone, C.M. (2015) Compositionally Controlled Volatile
681 Content of Nominally Volatile-Free Minerals in the Continental Upper Mantle of
682 Southern Gondwana (Patagonia & W. Antarctica). American Geophysical Union Fall
683 Meeting, San Francisco, Abstract #V51I-02.
684 Rosenthal, A., Hauri, E.H., and Hirschmann, M.M. (2015) Experimental determination of C, F,
685 and H partitioning between mantle minerals and carbonated basalt, CO_2/Ba and CO_2/Nb
686 systematics of partial melting, and the CO_2 contents of basaltic source regions. Earth and
687 Planetary Science Letters, 412, 77–87.
688 Rossman, G., 2006. Analytical Methods for Measuring Water in Nominally Anhydrous Minerals.
689 Reviews in Mineralogy and Geochemistry, 62, 1–28.
690 Sarafian, E., Evans, R.L., Collins, J.A., Elsenbeck, J., Gaetani, G.A., Gaherty, J.B., Hirth, G.,

691 and Lizarralde, D. (2015) The electrical structure of the central Pacific upper mantle
692 constrained by the NoMelt experiment. Geochemistry, Geophysics, Geosystems, 16,
693 1115–1132.
694 Schlecter, E., Stalder, R., and Behrens, H. (2012) Electrical conductivity of H-bearing
695 orthopyroxene single crystals measured with impedance spectroscopy. Physics and
696 Chemistry of Minerals, 39, 531-541.
697 Smyth, J.R., Bell, D.R., and Rossman, G.R. (1991) Incorporation of hydroxyl in upper-mantle
698 clinopyroxenes. Nature, 351, 732-735.
699 Stalder, R., Klemme, S., Ludwig, T., and Skogby, H. (2005) Hydrogen incorporation in
700 orthopyroxene: interaction of different trivalent cations. Contributions to Mineralogy and
701 Petrology, 150, 473–485.
702 Stalder, R., Prechtel, F., and Ludwig, T. (2012) No site-specific infrared absorption coefficients
703 for OH-defects in pure enstatite. European Journal of Mineralogy, 24, 465-470.
704 Stolper, E., and Newman, S. (1994) The role of water in the petrogenesis of Mariana trough
705 magmas. Earth and Planetary Science Letters, 121, 293–325.
706 Tarassoff, P., and Gault, R.A. (1994) The Orford Nickel Mine, Quebec, Canada. Mineralogical
707 Record, 25, 327–345.
708 Tenner, T.J., Hirschmann, M.M., Withers, A.C., and Hervig, R.L. (2009) Hydrogen partitioning
709 between nominally anhydrous upper mantle minerals and melt between 3 and 5 GPa and
710 applications to hydrous peridotite partial melting. Chemical Geology, 262, 42–56.
711 Toplis, M.J., Libourel, G., and Carroll, M.R. (1994) The role of phosphorus in crystallisation
712 processes of basalt: An experimental study. Geochimica et Cosmochimica Acta, 58, 797-
713 810.

714 Turner, M., Ireland, T., Hermann, J., Holden, P., Padrón-Navarta, J.A., Hauri, E.H., Turner, S.
715 (2015) Sensitive high resolution ion microprobe – stable isotope (SHRIMP-SI) analysis
716 of water in silicate glasses and nominally anhydrous reference minerals. Journal of
717 Analytical Atomic Spectrometry, 30, 1706–1722.
718 Volpe, A.M., Macdougall, J.D., Lugmair, G.W., Hawkins, J.W., and Lonsdale, P. (1990) Fine-
719 scale isotopic variation in Mariana Trough basalts: evidence for heterogeneity and a
720 recycled component in backarc basin mantle. Earth and Planetary Science Letters, 100,
721 251–264.
722 Warren, J.M. (2016) Global variations in abyssal peridotite compositions. Lithos, 248-251, 193–
723 219.
724 Warren, J.M., and Hauri, E.H. (2014) Pyroxenes as tracers of mantle water variations. Journal of
725 Geophysical Research: Solid Earth, 119, 1851–1881.
726 Watson, E.B., Cherniak, D.J., and Holycross, M.E. (2015) Diffusion of phosphorus in olivine
727 and molten basalt. American Mineralogist, 100, 2053-2065.
728 Welsch, B., Hammer, J., and Hellebrand, E. (2014) Phosphorus zoning reveals dendritic
729 architecture of olivine. Geology, 42, 867-870.
730 Withers, A.C., Bureau, H., Raepsaet, C., and Hirschmann, M.M. (2012) Calibration of infrared
731 spectroscopy by elastic recoil detection analysis of H in synthetic olivine. Chemical
732 Geology, 334, 92–98.
733 Withers, A.C., Hirschmann, M.M., and Tenner, T.J. (2011) The effect of Fe on olivine H_2O
734 storage capacity: Consequences for H_2O in the martian mantle. American Mineralogist,
735 96, 1039–1053.
736 Witt-Eickschen, G., and O'Neill, H.St.C. (2005) The effect of temperature on the equilibrium

distribution of trace elements between clinopyroxene, orthopyroxene, olivine and spinel in upper mantle peridotite. Chemical Geology, 221, 65–101.

Wright, K., and Catlow, C.R.A. (1994) A Computer Simulation Study of (OH) Defects in Olivine. Physics and Chemistry of Minerals, 20, 515–518.

Xia, Q.-K., Hao, Y., Li, P., Deloule, E., Coltorti, M., Dallai, L., Yang, X., and Feng, M. (2010) Low water content of the Cenozoic lithospheric mantle beneath the eastern part of the North China Craton. Journal of Geophysical Research, 115, B07207.

Xia, Q.-K., Hao, Y.-T., Liu, S.-C., Gu, X.-Y., and Feng, M. (2013) Water contents of the Cenozoic lithospheric mantle beneath the western part of the North China Craton: Peridotite xenolith constraints. Gondwana Research, 23, 108–118.

Yang, X.-Z., Xia, Q.-K., Deloule, E., Dallai, L., Fan, Q.-C., and Feng, M. (2008) Water in minerals of the continental lithospheric mantle and overlying lower crust: A comparative study of peridotite and granulite xenoliths from the North China Craton. Chemical Geology, 256, 33–45.

Yu, Y., Xu, X.-S., Griffin, W.L., O'Reilly, S.Y., and Xia, Q.-K. (2011) H_2O contents and their modification in the Cenozoic subcontinental lithospheric mantle beneath the Cathaysia block, SE China. Lithos, 126, 182–197.

Figure captions

Figure 1: Depiction of pyroxene major element compositions on the pyroxene quadrilateral. Orthopyroxenes fall in the bottom left corner, near enstatite, while clinopyroxenes cluster near the upper left, near diopside. Data from this study are shown as red circles. The grey data points of the background field are from the Warren (2016) abyssal peridotite database.

760

761 **Figure 2:** Water measurements in pyroxene reference materials displayed as box-and-whisker
762 plots of all analyses within a sample that were not removed by the data reduction process. The
763 median of the data is displayed as a red line, and the first and third quartiles define the edges of
764 the box. The whiskers extend to the maximum and minimum analyses to show the full range of
765 water concentrations measured for each sample.

766

767 **Figure 3:** Fluorine and phosphorus measurements in pyroxene reference materials displayed as
768 box-and-whisker plots. For an explanation of the plot style, see Figure 2.

769

770 **Figure 4:** Example of fluid inclusions in an orthopyroxene grain in a thin section of 116610-29.
771 Image taken in plane-polarized transmitted light.

772

773 **Figure 5:** Comparison of calibration lines for orthopyroxene produced by the DTM standards
774 (Koga et al. 2003; Aubaud et al. 2007) and the reference materials presented in this study, with
775 concentration on the y-axis in ppm and the counts ratio $^{16}O^{1}H/^{30}Si$ on the x-axis. Samples were
776 run on the Stanford Cameca NanoSIMS 50L. Error bars are 1σ. For water concentration in the
777 reference materials from this study, the propagated uncertainty (Table 4) is used. Uncertainty in
778 the counts ratios is the standard deviation of 2-3 repeat measurements on the same grain. The
779 calibration lines produced by the two sets of calibration materials fall within error of each other
780 and are in fact nearly coincident.

781

782 **Figure 6:** Comparison of SIMS data collected by this study and FTIR measurements collected

783 by Peslier et al. (2002). Error bars are 1σ for both SIMS and FTIR, using the propagated
784 uncertainty in Table 4 for the SIMS data. The black line is the 1:1 correspondence line for the
785 two techniques.
786
787 **Figure 7:** Partitioning behavior between orthopyroxene and clinopyroxene for water (top),
788 fluorine (middle), and phosphorus (bottom). For all plots, data from this study are red triangles,
789 data from previous studies on natural samples are grey triangles, and experimental data are blue
790 circles. The partition coefficient for all natural samples, including those from this study, is shown
791 as a black dashed line, while the experimental partition coefficient is shown as a blue dashed
792 line. 1σ uncertainties in the volatile content for data from this study are shown unless smaller
793 than the symbol. Uncertainties in the partition coefficients are 1σ. See text for references.
794
795 **Appendix**
796 The basalt glass standard ALV-519-4-1 is used to track and correct for instrumental drift
797 and bias over the course of a session. For simplicity, the following steps are described for water,
798 but fluorine and phosphorus count ratios can be substituted for OH/Si for reducing these
799 elements.
800 The first correction accounts for instrumental drift over the course of a day, or
801 occasionally multiple days. The count ratio $^{16}O^{1}H/^{30}Si$ for ALV-519-4-1 is plotted against
802 analysis number and fit with a linear regression of the form, $y(x) = mx + b$, where y is the count
803 ratio $^{16}O^{1}H/^{30}Si$ and x is analysis number (Figure A1a). This regression is then used to calculate
804 percent change as a function of analysis number, $P(x) = y(x) / y(1)$.
805 While $P(x)$ is not linear, it is very close to linear over the number of analyses one can

gather in a single day. For simplicity, we approximated $P(x)$ as linear, thus forming the equation $P(x) = m_p x + b_p$. This allows P to be calculated based purely on analysis number, independent of the exact values of $y(x)$. P can then be applied to all unknown data (α_{raw}), including the ALV-519-4-1 data, as

$$\alpha'(x) = \alpha_{raw}(x) * P(x) = \alpha_{raw}(x) * (m_p x + b). \quad (1)$$

After these calculations, corrected $^{16}O^{1}H/^{30}Si$ values for ALV-519-4-1 should have a standard deviation of <10% (Figure A1b).

This drift correction accounts for differences of the course of a day, but it does not account for any differences between days nor any differences between mounts since each linear correction is referenced to the start of that day. In order to account for the differences between days and between mounts, a K-factor correction (K) is calculated. The K-factor is equal to the average $^{16}O^{1}H/^{30}Si$ count ration of ALV-519-4-1 on the standard mount divided by the average $^{16}O^{1}H/^{30}Si$ count ratio of ALV-519-4-1 on the unknown mount. The K-factor correction is then applied to all α' data from the Equation 1 as

$$\alpha''(x) = \alpha'(x) * K \quad (2)$$

where α'' represents the data after both corrections. The average count ratio of ALV-519-4-1 in α'' should now have a standard deviation of <10% across data from every day and on every mount from the session (Figure A1c).

Appendix Figure Caption:

Figure A1: Example set of analyses of ALV-519-4-1 from one day of the January 2016 session, shown at each step of the instrumental drift/bias corrections described. For each plot, the blue dots are individual analyses of ALV-519-4-1 on the unknown mount, the solid red line is the

829 linear least-squares solution to those data as a function of analysis number, and the dashed red
830 line is the average value for ALV-519-4-1 on the standard mount. Raw data before any
831 correction are shown in (a), drift-corrected data are shown in (b), and data after all corrections
832 are shown in (c). The x- and y-scales are the same for all plots.
833
834

835
836 **Tables**

837 **Table 1**: **Description of samples**

838 Previous work on both major element chemistry and water content is included in the reference
839 column. Samples with Smithsonian (SMNH) ID numbers were provided by the Department of
840 Mineral Sciences, Smithsonian Institution. References: [1] Peslier et al. (2002), [2] Luhr and
841 Aranda-Gomez (1997), [3] Harvey et al. (2012), [4] Brandon and Draper (1996).

Sample	SMNH ID	Locality	Lithology	Selected minerals	Refs
	109426-1	Salt Lake Craters, HI	Lherzolite xenolith	opx	
BCN-200	116610-26	San Quintin Volcanic Field, Mexico	Lherzolite xenolith	opx	1, 2
BCN-203	116610-29	San Quintin Volcanic Field, Mexico	Lherzolite xenolith	opx	1, 2
DGO-160	116610-18	Durango Volcanic Field, Mexico	Lherzolite xenolith	cpx, opx	1, 2
DGO-166	116610-21	Durango Volcanic Field, Mexico	Lherzolite xenolith	cpx, opx	1, 2
KH03-4		Kilbourne Hole, NM	Lherzolite xenolith	cpx, opx	3
KH03-27		Kilbourne Hole, NM	Lherzolite xenolith	cpx, opx	3
PR-7-2	117322-242	Premier Kimberlite, Transvaal, Africa	Kimberlite chrome diopside megacryst	cpx	
PR-7-5	117322-245	Premier Kimberlite, Transvaal, Africa	Kimberlite enstatite megacryst	opx	
SC-J1		San Carlos, AZ	Lherzolite xenolith	cpx	
Sim-9c		Simcoe Volcano, WA	Lherzolite xenolith	opx	1, 4
Sim-24		Simcoe Volcano, WA	Lherzolite xenolith	opx	1, 4
SLP-101	116610-14	Ventura Volcanic Field, Mexico	Lherzolite xenolith	cpx	1, 2

SLP-108	117213-5	Ventura Volcanic Field, Mexico	Clinopyroxenite in lherzolite xenolith	cpx, opx	
SLP-114	116610-10	Ventura Volcanic Field, Mexico	Harzburgite xenolith	opx	1, 2
SLP-142	116610-5	Santa Domingo Volcanic Field, Mexico	Lherzolite xenolith	cpx, opx	1, 2
SLP-402	116610-15	San Quintin Volcanic Field, Mexico	Lherzolite xenolith	cpx, opx	1, 2
SLP-403	116610-16	San Quintin Volcanic Field, Mexico	Lherzolite xenolith	cpx, opx	1, 2
SMC31139		Orford Nickel Mine, Quebec, Canada	Diopside	cpx	

842

843

844

845 **Table 2: Composition of DTM basaltic glass standards**

846 Concentrations of SiO_2 in weight percent. Concentrations of volatiles in ppm by weight. 1σ
847 uncertainties for water concentrations in ppm by weight. References: [1] Hauri et al. (2002), [2]
848 Bryan and Moore (1977), [3] Stolper and Newman (1994), [4] Volpe et al. (1990), [5] Hawkins
849 et al. (1990)

Sample	**SiO_2 (wt%)**	**H_2O (ppm)**	**F (ppm)**	**P (ppm)**	**References**
ALV-519-4-1	49.07	1700 (43)	95	302	1, 2
WOK-28-3	49.77	4900 (245)	185	545	1, 3, 5
ALV-1654-3	56.67	10000 (500)	975	2840	
ALV-1833-11	51.13	11700 (585)	195	786	1, 3, 4, 5
ALV-1846-12	50.75	15800 (790)	288	786	1, 3, 4, 5
ALV-1833-1	50.33	19800 (990)	446	1095	1, 3, 4

850

851

852 **Table 3: Water concentrations in DTM pyroxene standards**

853 Concentrations and 1σ uncertainties in ppm by weight. References: [1] Koga et al. (2003), [2]

854 Aubaud et al. (2007), [3] Bell et al. (1995), [4] Bell et al. (2004).

Sample	Mineral	H_2O (ppm)	References
A288	opx	44 (8)	1
India Enstatite	opx	141 (7)	1, 2
KBH-1	opx	217 (11)	1, 2, 3
ROM-273-OG2	opx	263 (13)	2, 4
ROM-271-DI10	cpx	195 (10)	2, 4
PMR-53	cpx	268 (14)	1, 2, 3
ROM-271-DI16	cpx	439 (22)	2, 4
ROM-271-DI21	cpx	490 (25)	2, 4

855

856

857 **Table 4: Volatile concentrations in pyroxene reference materials**

858 All concentrations and uncertainties given in ppm by weight. The two uncertainties given for each volatile are described in the text.

859 The number of analyses presented in this table represents the number of analyses that passed all data reduction tests. The percent of

860 analyses that passed the data reduction tests is also presented in the same column.

			Water			Fluorine			Phosphorus		
Sample	**Grains**	**Analyses (% good)**	**Conc. (ppm)**	**Std. Dev. (ppm)**	**Prop. 1σ (ppm)**	**Conc. (ppm)**	**Std. Dev. (ppm)**	**Prop. 1σ (ppm)**	**Conc. (ppm)**	**Std. Dev. (ppm)**	**Prop. 1σ (ppm)**
Orthopyroxene											
116610-29	2	25 (92%)	62	4	5	15.1	0.6	0.8	1.1	0.2	0.2
Sim-9c	2	17 (100%)	82	6	7	11.4	0.6	0.7	1.6	2.2	2.2
Sim-24	2	13 (87%)	110	7	8	14.8	0.4	0.7	b.d.		
116610-18	4	29 (91%)	119	10	11	22.7	1.1	1.4	1.3	0.2	0.2
116610-10	5	47 (100%)	128	12	12	17.4	1.0	1.2	0.5	0.1	0.1
117213-5	2	19 (95%)	169	9	11	4.5	0.2	0.3	3.3	0.3	0.3
KH03-27	9	104 (80%)	182	18	19	14.8	0.7	0.9	1.5	0.3	0.3
117322-245	2	14 (88%)	211	10	12	27.4	0.9	1.4	4.3	0.2	0.3
116610-21	2	26 (87%)	215	20	21	9.0	0.4	0.5	5.0	0.5	0.6
KH03-4	6	48 (96%)	216	12	14	25.0	0.9	1.3	10.6	0.8	0.9
116610-15	6	48 (91%)	234	21	22	50.3	2.2	2.9	10.0	1.6	1.7

116610-26	2	20 (100%)	237	19	20	9.1	0.6	0.7	2.5	0.5	0.5
109426-1	2	16 (84%)	241	14	15	22.0	0.9	1.2	18.6	11.2	10.9
116610-16	5	41 (95%)	264	26	28	23.6	1.1	1.4	6.7	1.0	1.0
116610-5	2	16 (89%)	309	26	27	3	0.2	0.2	1.8	0.2	0.2
Clinopyroxene											
SMC31139	4	30 (80%)	5	8	8	0.5	0.3	0.3	b.d		
SC-J1	6	43 (93%)	62	4	9	26.0	1.2	1.6	30.9	14.6	14.5
117322-242	6	25 (63%)	127	5	16	69.5	1.8	3.3	13.0	1.1	1.3
116610-18	5	29 (88%)	199	13	27	54.0	2.0	3.0	3.6	0.8	0.8
117213-5	4	28 (90%)	315	15	40	13.0	1.7	1.7	11.1	0.6	0.8
116610-21	2	16 (94%)	354	28	50	23.5	1.1	1.4	15.5	1.3	1.5
116610-14	4	19 (83%)	356	22	48	57.8	1.0	2.5	72.8	14.0	14.2
KH03-27	7	46 (96%)	367	18	49	39.4	1.5	2.2	5.3	0.5	0.6
116610-15	4	21 (100%)	441	31	61	118.2	1.8	5.0	46.6	1.7	3.1
KH03-4	4	26 (96%)	427	25	59	64.8	2.2	3.3	38.0	1.0	2.3
116610-16	2	19 (95%)	490	33	66	58.8	2.4	3.2	29.5	3.0	3.3
116610-5	2	8 (80%)	544	49	79	7.8	0.2	0.4	7.8	0.2	0.5

861

Figure 1

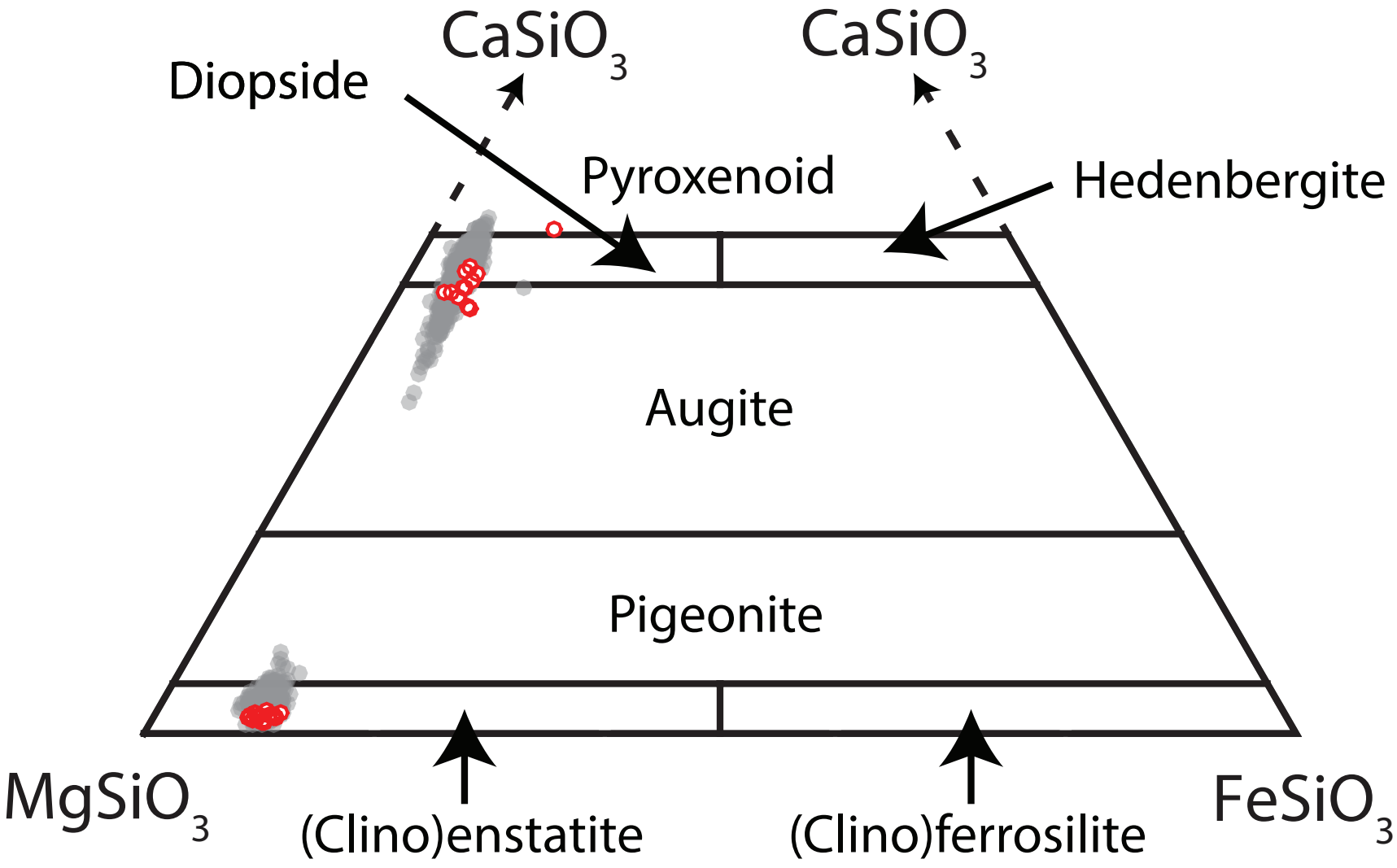
CaSiO3
CaSiO3
Diopside
Pyroxenoid
Hedenbergite
Augite
Pigeonite
MgSiO3
(Clino)enstatite
(Clino)ferrosilite
FeSiO3

Figure 2

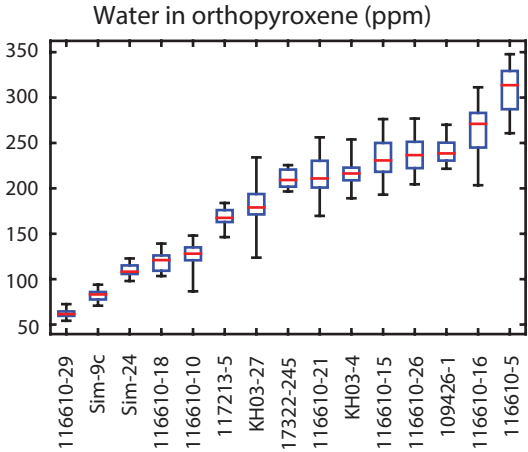
Water in orthopyroxene (ppm)
350
300
250
200
150
100
50
116610-29
Sim-9c
Sim-24
116610-18
116610-10
117213-5
KH03-27
117322-245
116610-21
KH03-4
116610-15
116610-26
109426-1
116610-16
116610-5

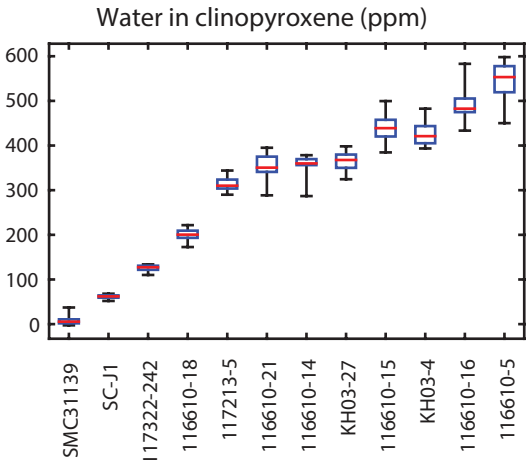
Water in clinopyroxene (ppm)
600
500
400
300
200
100
0
SMC31139
SC-J1
117322-242
116610-18
117213-5
116610-21
116610-14
KH03-27
116610-15
KH03-4
116610-16
116610-5

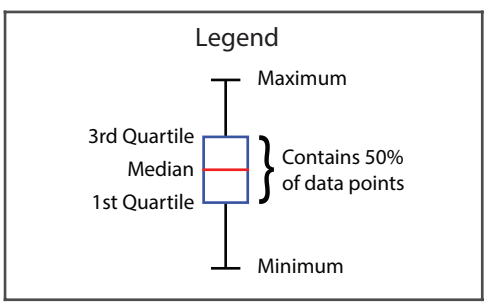
Legend
Maximum
3rd Quartile
Median
1st Quartile
Contains 50%
of data points
Minimum

Figure 3

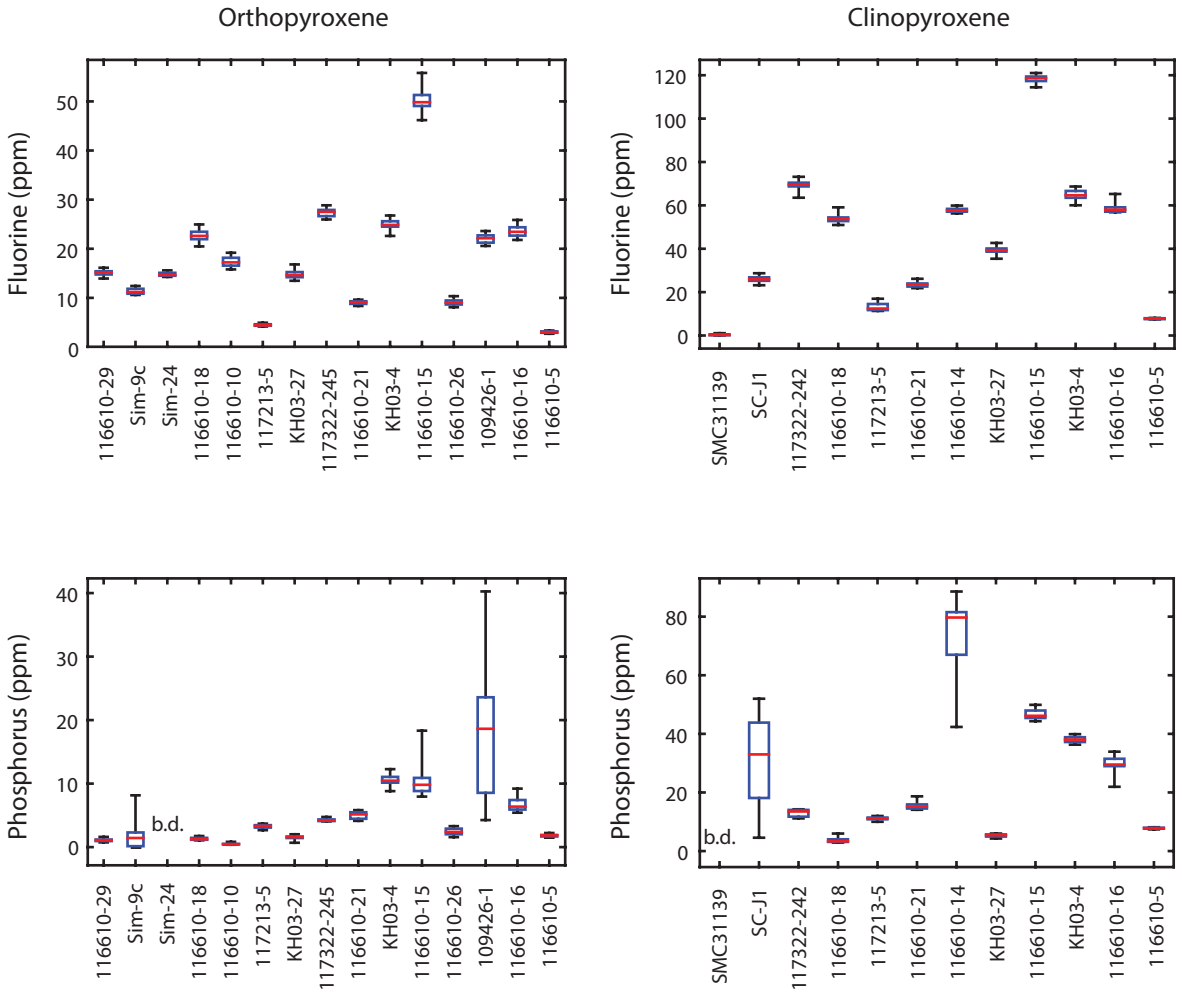
Orthopyroxene
Clinopyroxene
Fluorine (ppm)
Phosphorus (ppm)
b.d.
116610-29
Sim-9c
Sim-24
116610-18
116610-10
117213-5
KH03-27
117322-245
116610-21
KH03-4
116610-15
116610-26
109426-1
116610-16
116610-5
SMC31139
SC-J1
117322-242
116610-14

Figure 4

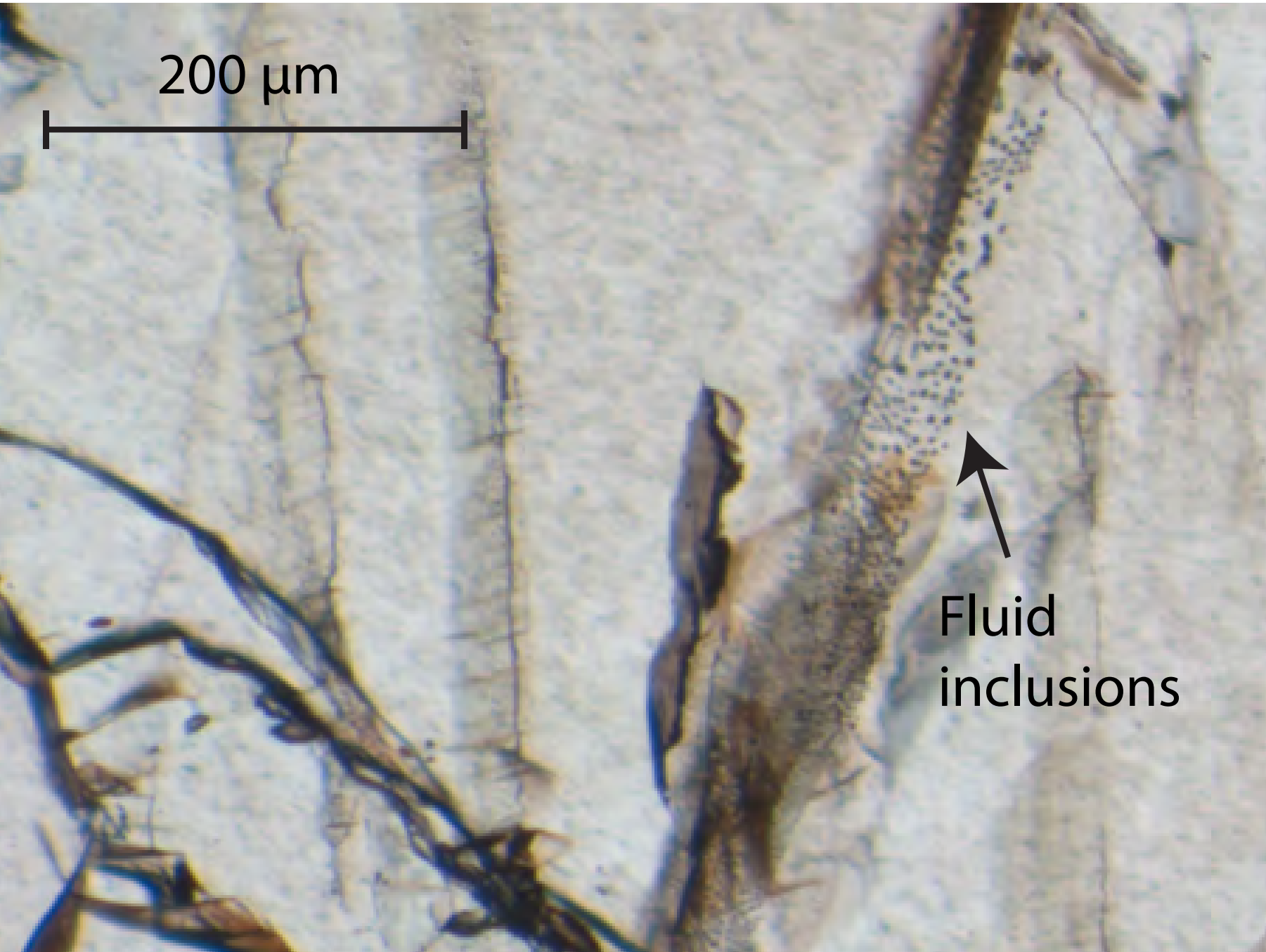

Figure 5

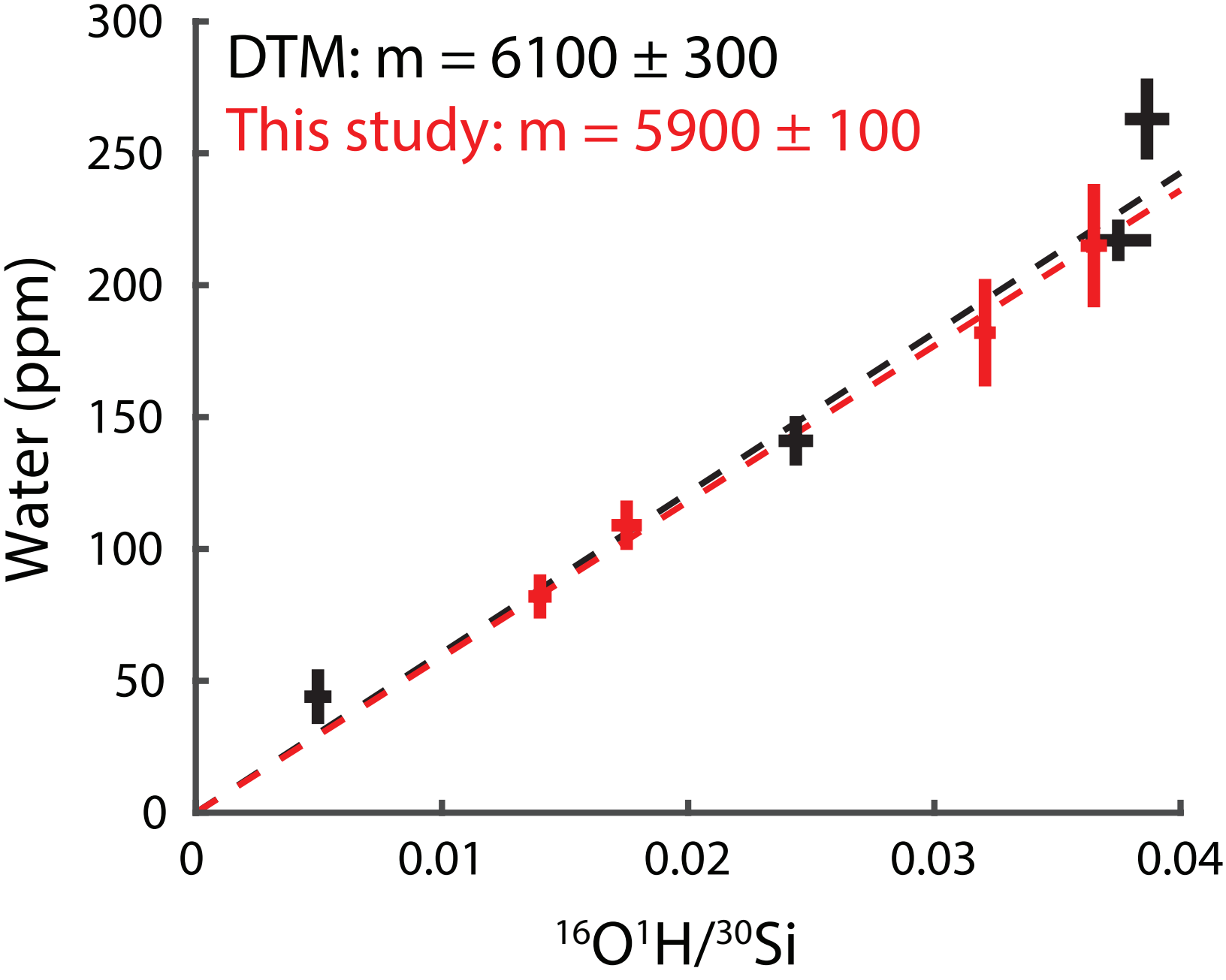
DTM: m = 6100 ± 300
This study: m = 5900 ± 100
Water (ppm)
300
250
200
150
100
50
0
0
0.01
0.02
0.03
0.04
16O1H/30Si

Figure 6

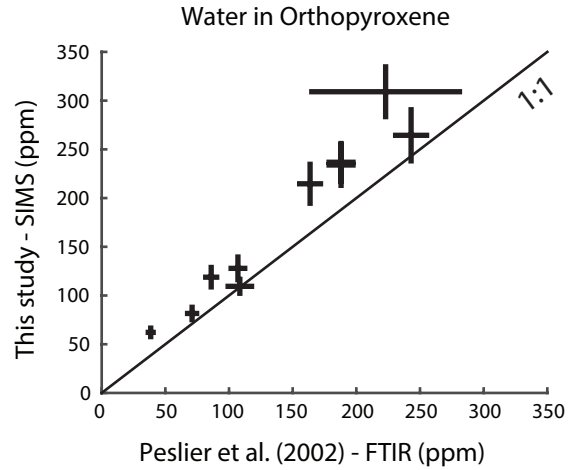
Water in Orthopyroxene
This study - SIMS (ppm)
Peslier et al. (2002) - FTIR (ppm)
1:1
0
50
100
150
200
250
300
350

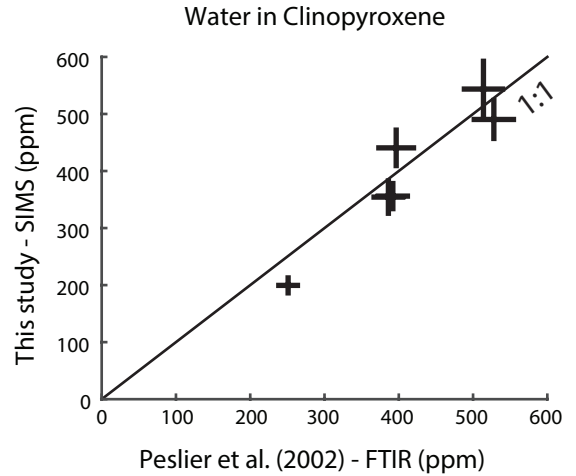
Water in Clinopyroxene
This study - SIMS (ppm)
Peslier et al. (2002) - FTIR (ppm)
1:1
0
100
200
300
400
500
600

Figure 7

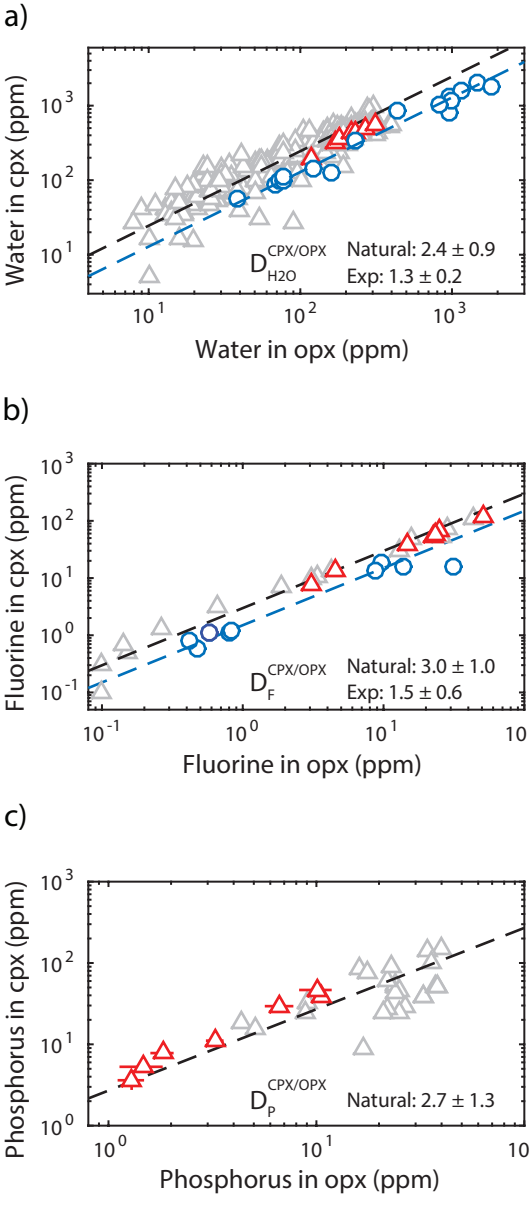
a)
Water in cpx (ppm)
Water in opx (ppm)
$D_{H2O}^{CPX/OPX}$
Natural: 2.4 ± 0.9
Exp: 1.3 ± 0.2
b)
Fluorine in cpx (ppm)
Fluorine in opx (ppm)
$D_{F}^{CPX/OPX}$
Natural: 3.0 ± 1.0
Exp: 1.5 ± 0.6
c)
Phosphorus in cpx (ppm)
Phosphorus in opx (ppm)
$D_{P}^{CPX/OPX}$
Natural: 2.7 ± 1.3

Figure A1

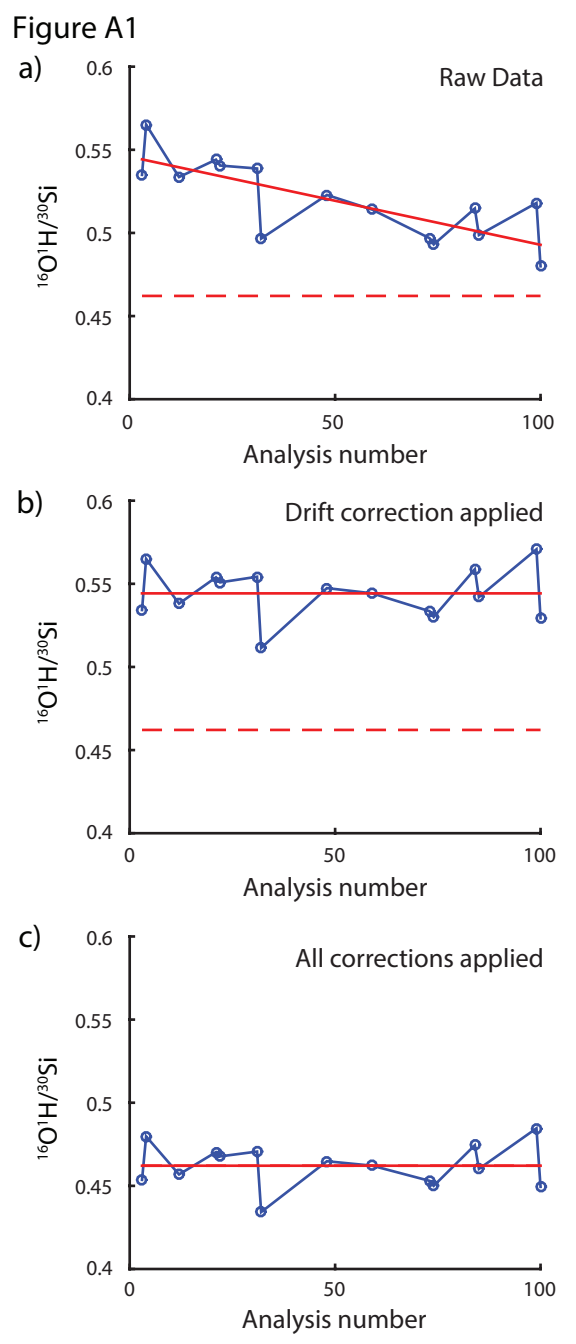
a)
Raw Data
$^{16}O^1H/^{30}Si$
0.6
0.55
0.5
0.45
0.4
0
50
100
Analysis number
b)
Drift correction applied
$^{16}O^1H/^{30}Si$
0.6
0.55
0.5
0.45
0.4
0
50
100
Analysis number
c)
All corrections applied
$^{16}O^1H/^{30}Si$
0.6
0.55
0.5
0.45
0.4
0
50
100
Analysis number